Cold Regions Science and Technology, 19 (1991) 261–273
Elsevier Science Publishers B.V., Amsterdam

Seasonal changes in sea ice optical properties during fall freeze-up

Donald K. Perovich
United States Army, Cold Regional Research and Engineering Laboratory, 72 Lyme Road, Hanover, NH 03755-1290, USA

(Received August 6, 1990; accepted after revision September 14, 1990)

ABSTRACT

Perovich, D.K., 1991. Seasonal changes in sea ice optical properties during fall freeze-up. *Cold Reg. Sci. Technol.*, 19: 261–273.

During the seasonal transition from summer to winter conditions, a sea ice cover undergoes a profound transformation. As the air temperature drops, the ice cools, the brine volume decreases, melt ponds freeze, new ice forms in areas of open water, and the surface becomes snow-covered. There is a corresponding change in the optical properties of the ice cover with albedos increasing and transmittances decreasing. As part of the Coordinated Eastern Arctic Experiment (CEAREX), measurements of spectral albedos, reflectances and incident irradiances were made at visible and near-infrared wavelengths (400–1100 nm) during fall freeze-up. In general, albedos increased as freeze-up progressed, with the increase being most pronounced at shorter wavelengths. The greatest temporal changes occurred in a freezing lead where, in only a few days, albedos increased from 0.1 for open water to 0.9 for snow-covered young ice.

The evolution of the transmitted radiation field under the ice was estimated using a two-stream, multilayer radiative transfer model in conjunction with observations of ice morphology and thickness. Transmission decreased dramatically due to ice cooling, snowfall, and declining incident solar irradiances. Light transmission through young ice was two orders of magnitude greater than through snow-covered multiyear ice.

Introduction

The reflection, absorption and transmission of short-wave radiation by sea ice are important to a number of geophysical phenomena in the polar regions. The critical role played by short-wave radiation in the heat and mass balance of a sea ice cover is well established (Maykut and Untersteiner, 1971; Grenfell and Maykut, 1977; Maykut and Perovich, 1987). A knowledge of the spectral reflectance of snow and ice types is critical in the interpretation of visible and near-infrared wavelength remote sensing imagery (Dirmhirn and Eaton, 1975). The amount and the spectral composition of transmitted light can strongly affect primary productivity and other biological activity in and under a sea ice cover (Soo Hoo et al., 1987).

Understanding radiative transfer in sea ice is considerably complicated by the large spatial and temporal variability in the physical, and therefore the optical, properties of the medium. Over distances of tens of meters ice thicknesses can range from open water to thick pressure ridges, while surface conditions can include bare ice, ponded ice and snow-covered ice. On a smaller scale, sea ice has an intricate structure consisting of ice platelets, brine pockets, brine channels and air bubbles, all of which can have variable sizes and orientations. In addition, since sea ice is always at or near its salinity-determined freezing point, small changes in temperature can produce large changes in ice properties. For example, as sea ice warms, the brine volume increases and internal platelet boundaries become smoother, brine pockets enlarge and con-

nect and air bubbles in the ice are released and coalesce into large bubbles. All these changes act to reduce light scattering within the ice, causing a decrease in the albedo (Perovich and Grenfell, 1981).

Perhaps the most pronounced temporal change in the optical properties occurs during the seasonal transition from cold winter conditions to the warm summer melt period. The evolution of spectral albedos in Arctic sea ice during this transition period was studied in detail by Grenfell and Perovich (1984). They found a general decrease of approximately 0.2–0.5 in spectral albedo (400–100 nm) as melting began and the ice cover evolved from snow-covered ice, to bare ice, to blue ice and melt ponds. This process was quite rapid, occurring in only one to two weeks. Studying Antarctic sea ice, Buckley and Trodahl (1987) reported large decreases in light transmission during late spring as the ice cover warmed and brine drainage occurred, resulting in the formation of a highly scattering surface layer.

There is another, less studied, seasonal transition when summer ends and winter returns. As the air temperature drops, the ice cools internally, causing a reduction in the brine volume, while melt ponds freeze, new ice forms in areas of open water and the ice becomes snow-covered. A field program to investigate changes in the optical properties of the ice during this period was conducted as part of the drift phase of the Coordinated Eastern Arctic Experiment (CEAREX). In this experiment an ice-strengthened vessel, the "Polarbjorn", traveled north to 82°41′N, 32°32′E, where it was moored to a floe and then allowed to drift with the ice pack from September through November 1988. During this experiment, measurements were made of spectral incident and reflected irradiance and of the physical characteristics of the ice cover. These measurements were coupled with ice characterization information to estimate the photosynthetically active radiation (PAR) transmitted through the ice cover to the underlying water column between 16 September and 6 October.

Instruments and methods

The optical measurements were made with a Spectron Engineering SE590 field portable, data-logging spectroradiometer. It is lightweight (approximately 4 kg) and was designed with field use in mind. The only modification needed for arctic field use was to thermally insulate the controller package. The detector head uses a single diffraction grating to disperse the spectrum, which is imaged onto a 252-element photodiode array. By using this photodiode array, the instrument samples the entire spectral range simultaneously, giving fast measurement times. This feature is particularly useful when making measurements under conditions of varying incident irradiance. The wavelength range is from 370 to 1100 nm, with a dispersion of 2.8 nm per element and a spectral resolution of 8 nm full-width half-power. Since the detector is configured as a single diffraction grating with no blocking filters, there is a second-order contribution at all wavelengths greater than 740 nm (2×370). This contribution was removed from the data numerically by reducing values at wavelengths greater than 740 nm by 1.5% of the reading at one-half the wavelength. Lens adapters for the detector provide a 1°, 10° or 20° field of view for radiance measurements. A hemispherical diffuser with excellent cosine response was used for irradiance measurements. The instrument was calibrated against a National Bureau of Standards traceable standard lamp, allowing absolute values of radiance and irradiance to be determined.

Optical measurements were made at over 40 sites encompassing a variety of ice types and conditions. These sites included new ice forming in a lead, second-year ice, multi-year ice, a freezing melt pond, blue ice, drained white ice, bubbly white ice, dirty ice and snow-covered ice. We periodically revisited some of the sites to monitor temporal changes in albedo. At each of these sites spectral incident $F_0(\lambda)$ and reflected irradiance $F_r(\lambda)$ were measured, enabling spectral albedos $\alpha(\lambda)=F_r(\lambda)/F_0(\lambda)$ to be calculated. Typically, observed light levels below 400 nm and above 1000 nm were low, resulting in noisy irradiances and albedos. Because of this, only values from 400 to 1000 nm are reported. At a few sites observations of the angular distribution of reflected radiance were also made.

For albedo measurements the detector was mounted on the end of a 1.5-m rod so it would not be in the operator's shadow. A measurement pair

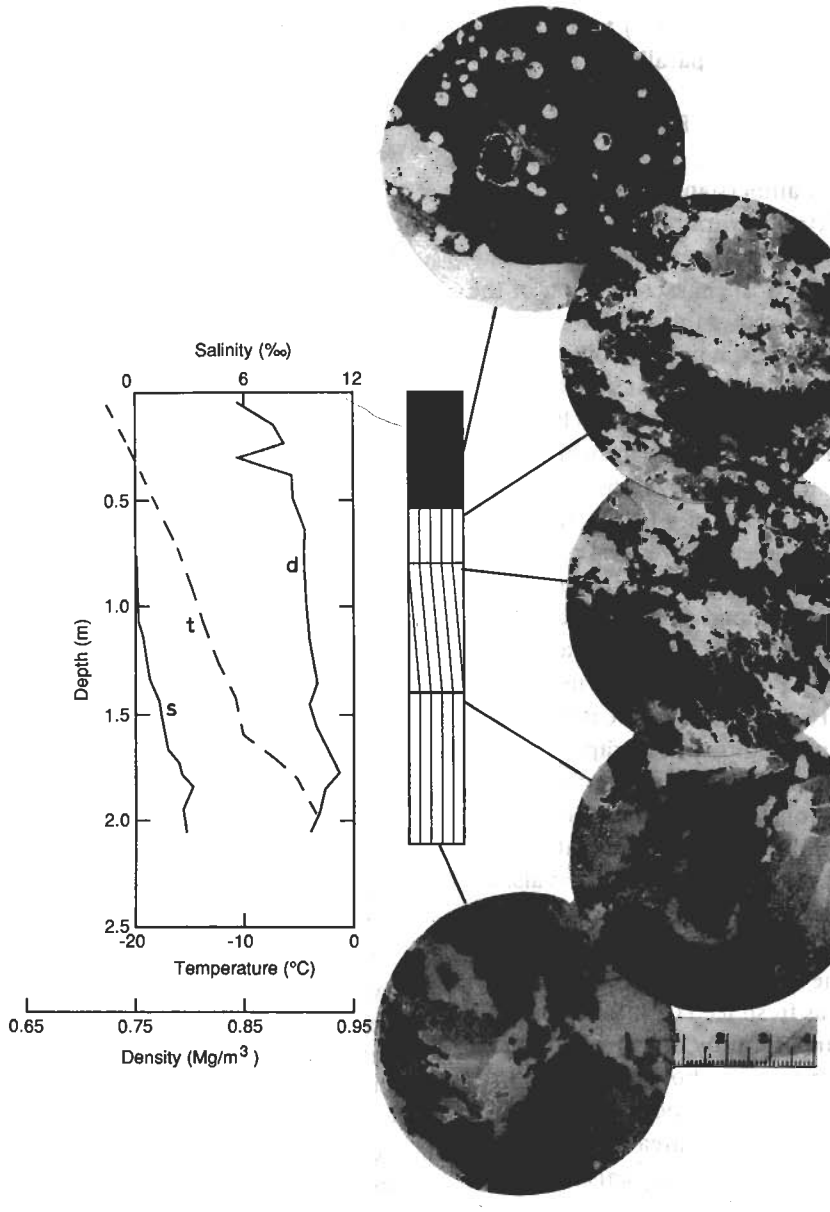

Fig. 1. Results from ice characterization for multi-year ice with a refrozen melt pond. Plotted are salinity (s), temperature (t) and density (d) as a function of depth. A sketch depicts the ice structure showing clear ice, columnar ice and inclined columnar ice. The photographs are horizontal thin sections from the indicated depths.

consisted of leveling the detector facing upward to measure the incident spectrum and then rotating downward 180° to measure the reflected spectrum. The temperature-sensitive controller package was housed in a thermally insulated rucksack. This configuration enabled spectral albedos to be readily surveyed over a large area.

At a few sites abbreviated measurements of the bidirectional reflectance function were made. This entailed determining the angular distribution of reflected radiances. For these measurements the cosine collector was replaced by a lens with a 1° field of view. The instrument was mounted on a bipod and reflected radiances were measured at 10° inter-

vals of elevation from nadir ($\theta=0°$) to near-horizontal ($\theta=80°$) at azimuths parallel to the direction of the sun ($\phi=0°$) and perpendicular to the direction of the sun ($\phi=90°$). Reference values of radiance were measured using a Spectralon white (0.98–0.99 albedo) Lambertian standard.

Because of the extreme variability in ice conditions, an important supplement to the optical measurements was the physical characterization of the snow and ice. For the snow, this consisted of the snow depth and a description of the snow stratigraphy including grain size and type. At selected sites, the sea ice structure was analyzed in detail by taking an 80-mm-diameter core completely through the ice. The method used to characterize the ice is described in detail by Tucker et al. (1987). A portion of the core was used to measure vertical profiles of ice salinity, temperature, and density, from which profiles of brine volume and porosity were computed. Vertical thin sections were prepared and viewed under crossed Polaroids to determine crystal types and sizes. Highlights of the ice petrographics were then documented by photographs of horizontal thin sections. This characterization is illustrated in Fig. 1 for the case of a multi-year, refrozen melt pond. Plotted are ice temperature, salinity and density measured at 0.10-m intervals, accompanied by a sketch depicting the ice structure and horizontal thin-section photographs from several levels within the ice. As the figure indicates, the upper half meter was fresh ice (0 ‰ salinity) from a refrozen pond, underlain by 1.6 m of columnar sea ice. The top thin-section photograph shows the clear fresh ice from the refrozen pond with some air bubbles apparent. The shaded areas in the photographs represent individual ice crystals, while the smaller, finer-scale features are individual ice platlets.

We supplemented these detailed site-specific measurements with ice thickness surveys and snow stake arrays to investigate areal variations in ice thickness and snow depth over horizontal scales of tens of meters. Thickness surveys consisted typically of an 11×11 grid of points at 5-m spacing where thicknesses were measured using a hot water drill. Snow-stake arrays were used to monitor snow accumulation and wind transport at four locations on thin lead ice, a smooth refrozen melt pond, multiyear ice and a pressure ridge.

Results

During the drift phase of CEAREX, the "Polarbjorn" was moored to a large (~1.5 km in diameter) composite multiyear floe, affording a wide variety of ice types for study. The floe was variegated, including second-year ice, old multi-year ice, dirty ice, ponded ice, and a 10-m-thick pressure ridge. Young ice types were found in a freezing lead adjacent to the floe. In addition to this spatial variability, there was considerable temporal variability as summer turned to winter. For example, in 1.6-m-thick multi-year ice the average ice temperature decreased from $-1.2°$ to $-3.2°$C between 18 September and 11 October, causing a reduction in average brine volume from 7 to 4%. Surface melt ponds refroze, as this cooling occurred. Even more significant from an optical perspective was the increase in snow depth. On 21 September the ice was predominantly bare with only a few patches of snow, but by 11 October most of the ice was covered by an 0.08–0.10-m-thick snowcover.

Albedos

Spectral albedos for several different "blue" and "white" ice types observed during the experiment are displayed in Fig. 2. Spectral albedos for (1) a melt pond (Grenfell and Maykut, 1977), (2) a blue refrozen melt pond with few bubbles (Fig. 1), (3) a bubbly blue refrozen melt pond, (4) gray-green ice, and (5) blue ice covered by 0.15 m of snow are presented in Fig. 2a. Uncertainties in spectral albedo are approximately 0.01–0.03. The shapes of the blue ice curves are all similar: maximum albedos from 400 to 500 nm then a decrease from 500 to 800 nm, followed by fairly constant values from 800 to 1000 nm. This spectral shape results from the transparency of water and ice at shorter wavelengths (Grenfell and Perovich, 1981, 1984; Smith and Baker, 1981). Albedos below 500 nm are governed primarily by the scattering properties of the underlying ice, while from 500 to 800 nm the albedo becomes increasingly insensitive to the under-

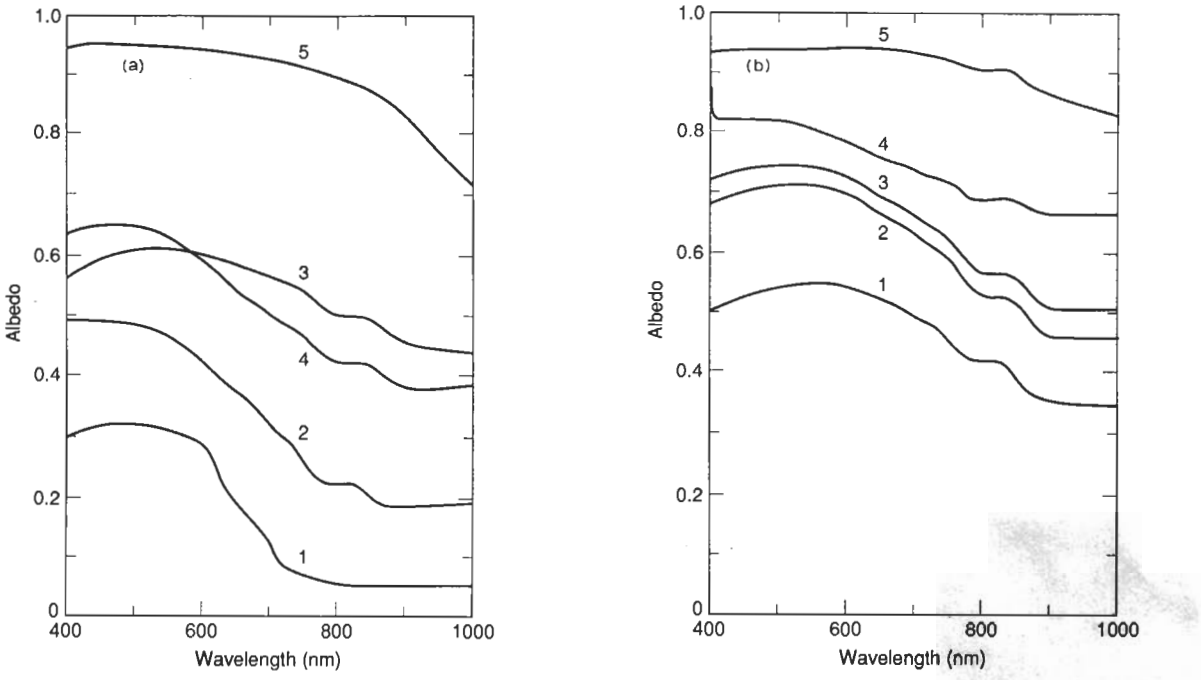

Fig. 2. Spectral albedos for (a) ponded ice types, and (b) white ice types. The blue ice types in Fig. 2a include (1) a 0.12-m-deep melt pond on blue ice (Grenfell and Maykut, 1977), (2) a blue refrozen pond with very few air bubbles, (3) a green refrozen melt pond, (4) a blue refrozen melt pond, and (5) blue ice with a 0.15-m snowcover. The white ice types plotted are (1) dirty ice, (2) smooth white ice, (3) rough white ice, (4) white ice with 0.02 m surface drained layer, and (5) a thick pressure ridge with a 0.40-m deep snowcover.

lying ice as the absorption in the surface layer becomes the dominant factor (Perovich and Grenfell, 1981). Above 800 nm the absorption in the surface layer is so great that only the upper few centimeters contribute to the albedo. For melt ponds the albedo from 800 to 1000 nm is determined by Fresnel reflection at the surface and therefore is independent of wavelength. The difference in magnitude between these three cases results from differences in the amount of scattering, with the melt pond having the fewest scatterers and the bubbly blue ice the most. As a melt pond freezes, air bubbles form in the ice, enhancing scattering, resulting in an increase in albedo. The more air bubbles deposited in the ice, the greater the scattering and the larger the albedo. Even more pronounced is the increase in albedo that occurs when the surface becomes snow-covered. The addition of 0.15 m of highly scattering snow (0.5–1.0 mm diameter loose rounded grains) increased the albedo by 0.3 to 0.6. The gray-green ice albedo is similar in magnitude to that of blue bubbly ice, but with the maximum shifted to 500–600 nm. The greenish color of this ice was the result of biological activity.

Spectral albedos summarizing white ice types are displayed in Fig. 2b. The lowest albedos were for "dirty", sediment-laden ice. The presence of the sediment, which is a good absorber but not a good scatterer, caused a reduction in albedo. There was an increase in albedo at all wavelengths from smooth white ice to rough white ice to drained white ice. While the interior ice structure was quite similar for these three cases, the surface layers were different. The albedo for rough white ice was higher than for smooth white ice due to the additional scattering from the small-scale roughness of the surface. The drained white ice case had a 0.02-m surface layer where the brine had drained, leaving a skeletal ice platelet structure with many air–ice interfaces. These interfaces caused considerable scattering, resulting in enhanced albedos. As was true for the blue ice cases, the presence of a snow cover increased the

albedo. The largest albedos were measured on a ridge with a 0.40-m-thick snow cover composed of 1–2 mm hexagonal snow crystals.

The most profound changes in albedo occurred in a freezing lead. Weller (1972) observed an increase in total albedo from 0.08 to 0.40 during the initial 0.3 m of ice growth. Schlosser (1988) found a sharp increase in spectral albedo during the initial growth phase of Antarctic sea ice. Ice conditions in a narrow freezing lead are illustrated in Fig. 3. The center of the lead is covered by a skim of frazil, while 30–50 mm of slush ice has accumulated near the edges. Adjacent to the lead is snow-covered young ice. A time series of spectral albedos for a freezing lead are shown in Fig. 4. The albedo of water is low, approximately 0.05–0.10, with wind roughening of the water causing a slight increase (Burt, 1954). For clear water, the albedo results from specular reflection at the surface and thus is essentially independent of wavelength from 400–1000 nm (Fig. 4, curve 1). Since the initial ice growth was under quiescent conditions, a thin skim of frazil formed in the lead as freezing commended, causing a slight increase in albedo (curve 2). As freezing continued the ice thickened to 0.03 m of nilas and spectral albedos increased to 0.2 (curve 3). Interestingly, the nilas albedos beyond 900 nm were lower than those of open water or the thin frazil skim. The nilas was

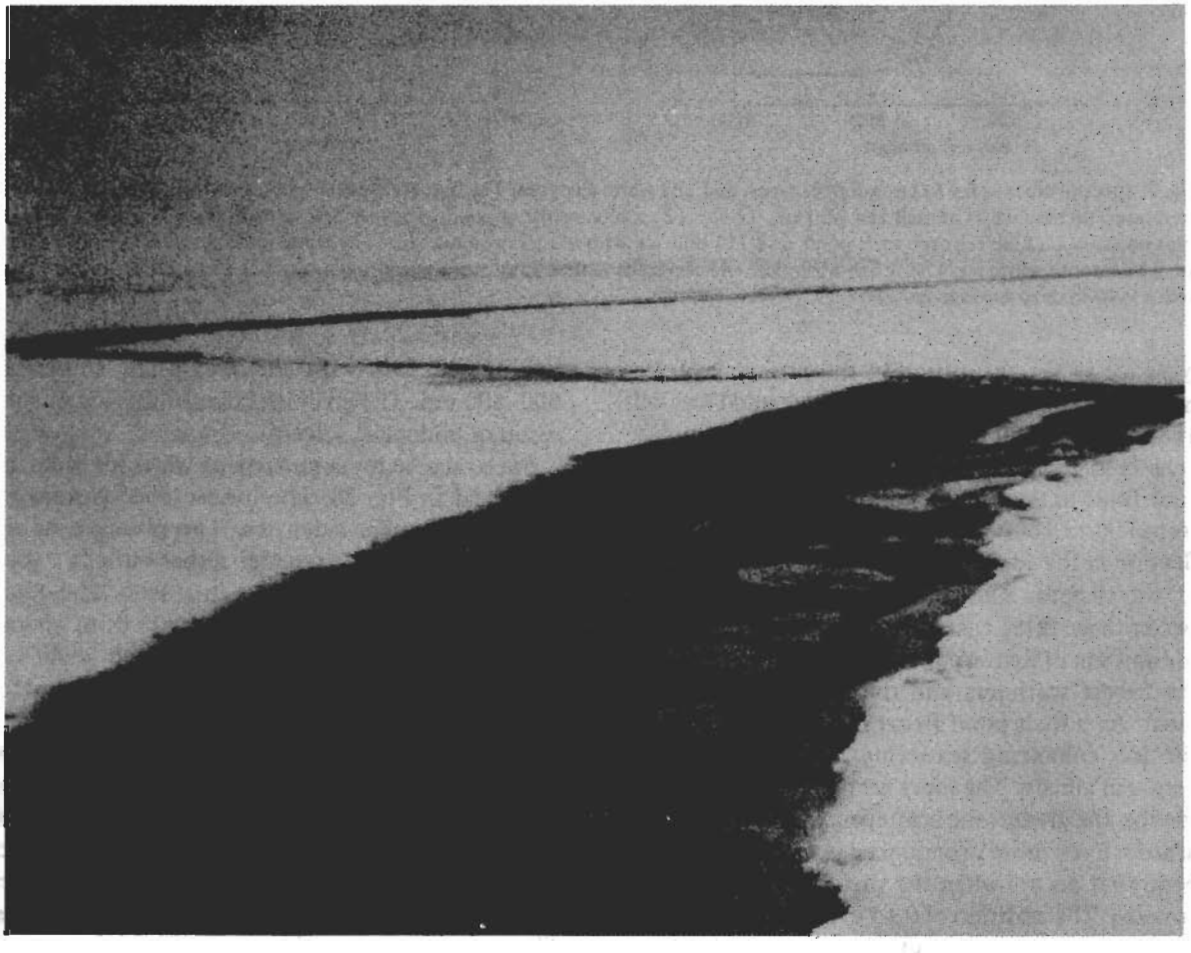

Fig. 3. Ice conditions in a freezing lead. The center of the lead is covered by a skim of frazil ice, while 30–50 mm of slush ice has accumulated near the edges.

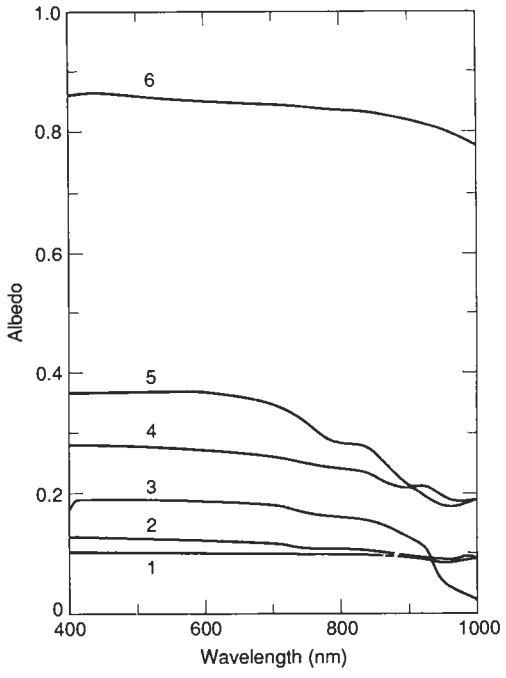

Fig. 4. Spectral albedos for new ice in a freezing lead. The curves are (1) wind-roughened water, (2) 2-mm-thick skim of frazil, (3) 0.03-m-thick nilas, (4) gray ice 0.05-m thick, (5) 0.20-m-thick ice with no snow, and (6) 0.20 m of young ice covered by 0.04 m of snow.

covered by a thin, smooth water layer, which gave less Fresnel reflection than the rough open water or frazil skim surfaces. Albedos continued to increase, particularly at shorter wavelengths, as the ice thickness increased to 0.05 m (curve 4) and 0.20 m (curve 5). Albedos were fairly constant at visible wavelengths (400–700 nm), giving the young ice a grayish appearance. Structurally, the upper top 0.05 m of the ice was composed of granular ice underlain by 0.15 m of columnar ice. Even a 10 mm snow-cover of 1 to 1.5-mm-long needles over 30 mm of 1-mm-diameter wet rounded grains (curve 6) caused a sharp increase in albedo, making the young ice optically indistinguishable from multi-year ice.

Because of the importance of surface-based albedo measurements in interpreting satellite imagery, a thematic mapper simulation (Table 1) was generated for the ice types displayed in Figs. 2 and 3. Following the convention of Grenfell and Perovich (1984) it was assumed that the signal seen by the satellite could be approximated by the product $\alpha_\lambda R_\lambda F_0(\lambda)$ under clear skies integrated over the appropriate wavelength region, where R_λ is the spectral instrument response of the thematic mapper. To avoid absolute calibration concerns, the results displayed in Table 1 were normalized by snow values (Fig. 2a, curve 5). The results indicate that band 1 affords the largest variation in signal among ice types. For young ice and white ice cases, bands 1–3 show very little discrimination.

Bidirectional reflectance function

The albedo is a measure of the reflected light integrated over the entire hemisphere and therefore consists of a diffuse and a direct component. Satellite sensors typically have narrow fields of view and thus do not measure albedo, but rather the reflected radiance at a particular angle (Taylor and Stowe, 1984). Therefore, in some cases it may be inappropriate to use albedos to interpret satellite imagery. In order to precisely analyze data from satellite radiometers, the bidirectional reflectance function (BDRF) of the surface must be known. The BDRF has units of steradians^{-1} and is defined (Warren, 1982) for a surface free of azimuthally dependent surface features as

$$R(\theta_0,\theta,\phi,\lambda) = \mathrm{d}I_r(\theta,\phi,\lambda)/\mu_0 \mathrm{d}F_0(\theta_0,\phi,\lambda)$$

where θ_0 is the solar zenith angle, θ is the detector zenith angle, ϕ is the azimuth angle between the sun and the detector, $\mu_0 = \cos(\theta_0)$, $F_0(\theta_0,\phi,\lambda)$ is the spectral incident irradiance and $I_r(\theta,\phi,\lambda)$ is the reflected spectral radiance. There have been several studies performed on the bidirectional reflectance properties of snow (Dirmhirn and Eaton, 1975; Kuhn, 1985; Steffen, 1987). Though there have been no field observations reported for sea ice, Schlosser (1988) conducted a laboratory study investigating azimuthal variations in reflectance for thin ice. Using white and red light she found a high degree of azimuthal anisotrophy for thin ice, which decreased as the ice grew thicker. Maximum values were found when the angel of reflection equaled the angle of incidence.

It was beyond the scope of this work to completely determine the BDRF for bare sea ice types; however, some limited measurements were made at a single solar zenith angle. Spectral measurements

TABLE I

Thematic mapper simulation for bands 1–4 using spectral albedo data

These are relative values normalized by the results from a thick snow cover case (Fig. 2a, curve 5)

Ice type	Curve	Band 1 450–520 nm	Band 2 52–600 nm	Band 3 630–690 nm	Band 4 760–900 nm
Fig. 2a					
Blue refrozen pond	2	0.52	0.48	0.39	0.24
Green refrozen pond	3	0.69	0.66	0.57	0.46
Bubbly refrozen pond	4	0.64	0.65	0.62	0.55
Fig. 2b					
Dirty white ice	I	0.57	0.58	0.55	0.45
Smooth white ice	2	0.75	0.75	0.70	0.58
Rough white ice	3	0.79	0.78	0.73	0.62
Drained white ice	4	0.87	0.85	0.80	0.76
Fig. 4					
Water	1	0.11	0.11	0.11	0.11
Frazil skim (2 mm)	2	0.14	0.13	0.13	0.12
Nilas (30 mm)	3	0.20	0.20	0.20	0.17
Gray ice (50 mm)	4	0.30	0.29	0.28	0.26
Young ice (200 mm)	5	0.39	0.39	0.38	0.30

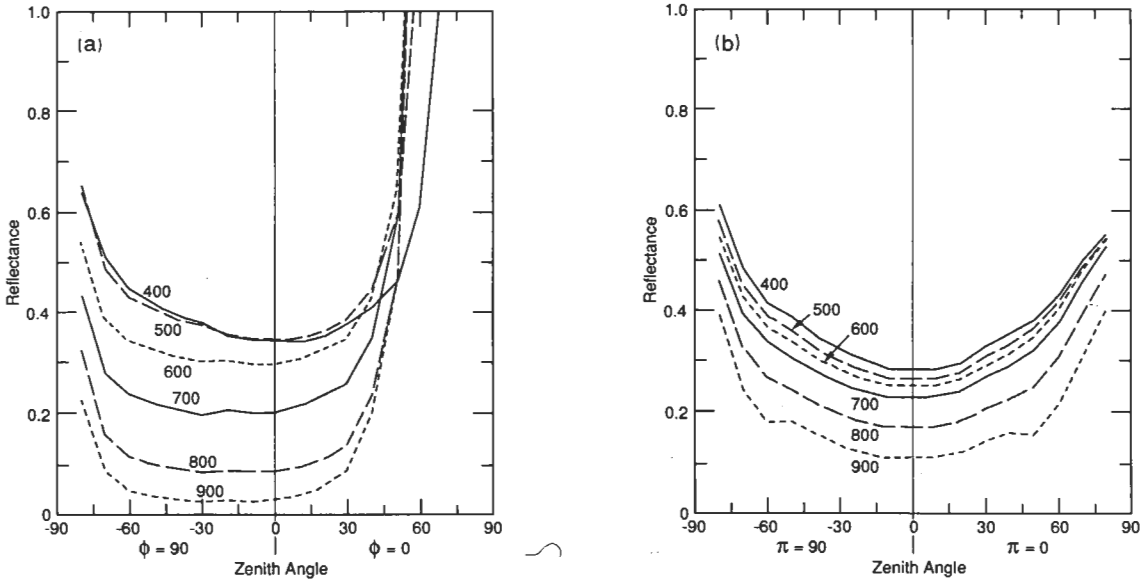

Fig. 5. Spectral values of the bidirectional reflectance function for (a) refrozen melt pond ($\theta_0=7°$) and (b) 0.2-m-thick young ice ($\theta_0=6°$).

are plotted in Fig. 5 for (a) a refrozen melt pond, and (b) 0.20-m young ice at nine detector zenith angles (0°, 10°, 20°, 30°, 40°, 50°, 60°, 70°, 80°) and azimuthal angels of 90° (perpendicular to sun) and 0° (looking towards the sun). The reflectance at (θ,ϕ) was computed by normalizing the observed reflected radiance from the surface by that from the reference standard.

The spectral dependence of reflectance is similar to that of albedo, exhibiting an overall decrease with increasing wavelength. The large increase in the refrozen melt pond reflectance at low sun angles for $\phi=0°$ was due to significant specular reflection off the smooth surface. This sharp increase was not seen for the young ice, which had a surface that was very rough on a small scale. For the refrozen pond, reflectances perpendicular to the sun ($\phi=90°$) were fairly constant for $\theta=0°$–$60°$, as was also the case for young ice for both $\phi=0°$ and $\phi=90°$. This finding is in agreement the visual observations of Grenfell and Perovich (1984) who noted that the color and contrast of snow and ice surface types are nearly independent of zenith angle from nadir to approximately 70°. While it is best to have the complete BDRF to interpret remote sensing data, albedos can provide a reasonable approximation for cases with rough ice surfaces and high zenith angle.

Incident irradiance

Spectral incident irradiances were computed by combining the incident spectra measured for the albedo calculations with the absolute calibration curve for the instrument. Results for two distinct cloud cases are presented in Fig. 6; (1) clear skies, and (2) complete overcast with solar disk not visible. Approximate error estimates are ±1% from 400–600 nm, ±5% from 600–800 nm, and 1% from 800–1000 nm. Maximum values are near 470 nm, in good agreement with previous observations (Gast, 1960; Iqbal, 1983). The spectral incident irradiance decreases with increasing cloudiness, and there was also a day-to-day downward trend during the experiment as the sun approached the horizon. The observed incident irradiance showed a combination of these two effects. Spectrally, the reduction in incident irradiance due to a cloud cover is greater at longer wavelengths. For example, in the clear sky case, 40% of the total energy between 400–1000 nm is contained between 700–1000 nm, compared to only 31% for complete overcast conditions.

Transmittance

During the early portion of the drift phase there was a strong algal bloom of Phaeocystis. Qualitatively this was observed as a fouling of oceanographic sensors and the ship's water filters. More quantitatively, concentrations of chlorophyll-A as high as 34 mg/m^3 were measured in the ice, indicating high productivity (D.A. Meese, pers. commun., 1989). As this bloom occurred, the days were growing shorter, the incident shortwave irradiance was steadily declining and snow was accumulating on the ice surface, all reducing light transmission to the ocean. Given this, it is surprising that there was sufficient light available under the ice for this productivity. Therefore the question arises: What were the light levels under the ice cover?

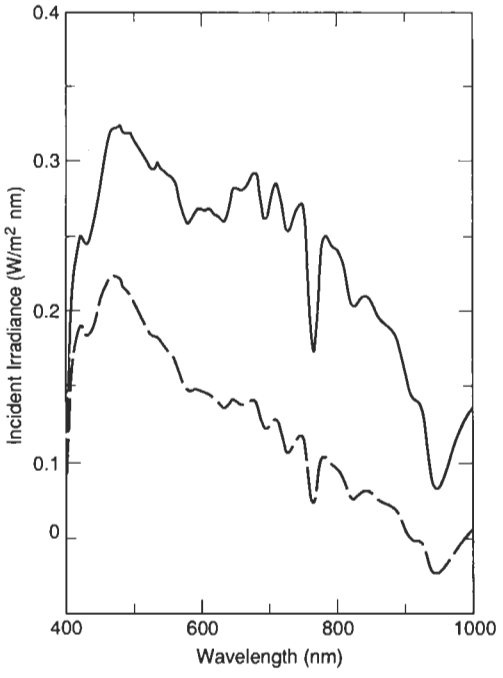

Fig. 6. Incident spectral irradiances for clear skies (solid line) (20 September 1988, solar elevation $\theta=5°$), and complete cloud cover, solar disk not visible (dashed line) (17 September, $\theta=9°$). The total irradiance integrated from 400–1000 nm was 141 W/m^2 for clear skies and 74 W/m^2 for complete overcast.

Since no measurements of transmitted lights were made, these questions will be addressed theoretically using a two-stream, multi-layer radiative transfer model for sea ice developed by Perovich (1989). The model calculates the upwelling and downwelling irradiance in each layer by solving the coupled first-order differential equations (Dunkle and Bevans, 1956; Perovich, 1989). Changes in

downwelling irradiance $F_{\downarrow}(z,\lambda)$ are due to absorption losses, scattering losses from the downwelling stream and scattering gains from the upwelling stream:

$$dF_{\downarrow}(z,\lambda) = -k_{\lambda}F_{\downarrow}(z,\lambda)dz - r_{\lambda}F_{\downarrow}(z,\lambda)dz + r_{\lambda}F_{\uparrow}(z,\lambda)dz \quad (1)$$

while changes in upwelling result from absorption losses, scattering gains from the downwelling stream and scattering losses from the upwelling stream:

$$dF_{\uparrow}(z,\lambda) = k_{\lambda}F_{\uparrow}(z,\lambda)dz - r_{\lambda}F_{\downarrow}(z,\lambda)dz + r_{\lambda}F_{\uparrow}(z,\lambda)dz \quad (2)$$

where z is the depth within the medium (increasing downward) and λ is the wavelength of the light. Scattering (r_{λ}) and absorption (k_{λ}) are treated through wavelength-dependent coefficients. Together the scattering and absorption coefficients define the extinction coefficient $\kappa_{\lambda} = (k_{\lambda}^2 + 2k_{\lambda}r_{\lambda})^{0.5}$. Equations 1 and 2 can be reformulated as uncoupled second-order differential equations with general solutions (Perovich, 1989):

$$F_{\downarrow}(z,\lambda) = A\sinh(\kappa_{\lambda}z) + B\cosh(\kappa_{\lambda}z) \quad (3)$$

$$F_{\uparrow}(z,\lambda) = C\sinh(\kappa_{\lambda}z) + D\cosh(\kappa_{\lambda}z) \quad (4)$$

A system of $4N$ equations (N being the number of layers) consisting of eqns. 3 and 4 applied at each layer interface plus boundary conditions is solved simultaneously to determine the constants A, B, C and D for each layer, from which spectral albedos and transmittances can be computed. The transmittance being the fraction of the incident irradiance transmitted through the ice. The input parameters for the model are easily observable quantities: (1) incident shortwave irradiance, (2) cloud cover, (3) ice thickness, (4) snow depth, and (5) a qualitative description of the ice structure (white ice, blue ice, melting ice, etc.). Given these parameters, the model calculates spectral albedos (α_{λ}), transmittance (T_{λ}) and photosynthetically active radiation (PAR) values. Spectral values can be integrated over wavelength to determine bulk albedo (α_B):

$$\alpha_B = \int \alpha_{\lambda}F_0(\lambda)d\lambda / \int F_0(\lambda)d\lambda$$

and transmittance (T_B):

$$T_B = \int T_{\lambda}F_0(\lambda)d\lambda / \int F_0(\lambda)d\lambda$$

Since biological activity is controlled by the number of photons of a particular wavelength, transmitted irradiance in biological studies is often presented in terms of photons of wavelength λ per unit area per time, rather than the more familiar watts per meter squared. The basic unit of irradiance is micro-einsteins per meter squared per second, where an einstein (E) is equal to the energy of a mole of photons of wavelength λ, $E_n = nhc/\lambda$, and n = Avogadro's number (6.025×10^{23}), h = Planck's constant (6.625×10^{-34} joule sec), and c = speed of light (3×10^{17} nm/sec). Total PAR is defined as the integral of E_n from 400 to 700 nm.

The transmitted radiation field from 16 September to 6 October was estimated by applying the multi-layer model to two distinct cases; multi-year ice and lead ice. These two cases represented a substantial portion of the local ice cover. The snow and ice characterization needed for the model was obtained from ice cores and thickness measurements, while daily incident irradiance and cloud conditions were obtained from meteorological records (Lackman et al., 1989). Input parameters and wavelength-integrated model results are summarized in Table 2. The 1.6-m thickness of the multi-year ice remained unchanged during this period, through the upper 0.60 m of the ice cooled substantially, with temperatures at a depth of 0.20 m decreasing from $-1.1°$ to $-5.1°$C. Lead conditions changed from open water on 16 September to 0.23-m thick ice with a 0.04-m snowcover on 6 October. At this time the young ice consisted of a 0.03-m-thick surface layer of granular ice underlain by columnar ice.

Estimates of spectral transmitted PAR (400–700 nm) from 16 September to 6 October for the young ice and the multi-year ice cases are presented in Fig. 7. The young ice is far more transparent than the multi-year ice, transmitting 100 times more light. In the young ice, there was an initial drop in transmitted PAR when the lead first began to freeze, followed by a steady decrease as the ice grew thicker and another large decrease once the surface became snow-covered. In the multi-year ice, there was a sharp reduction in transmitted PAR on 24–26 September due to a 0.04-m snowfall. This was followed

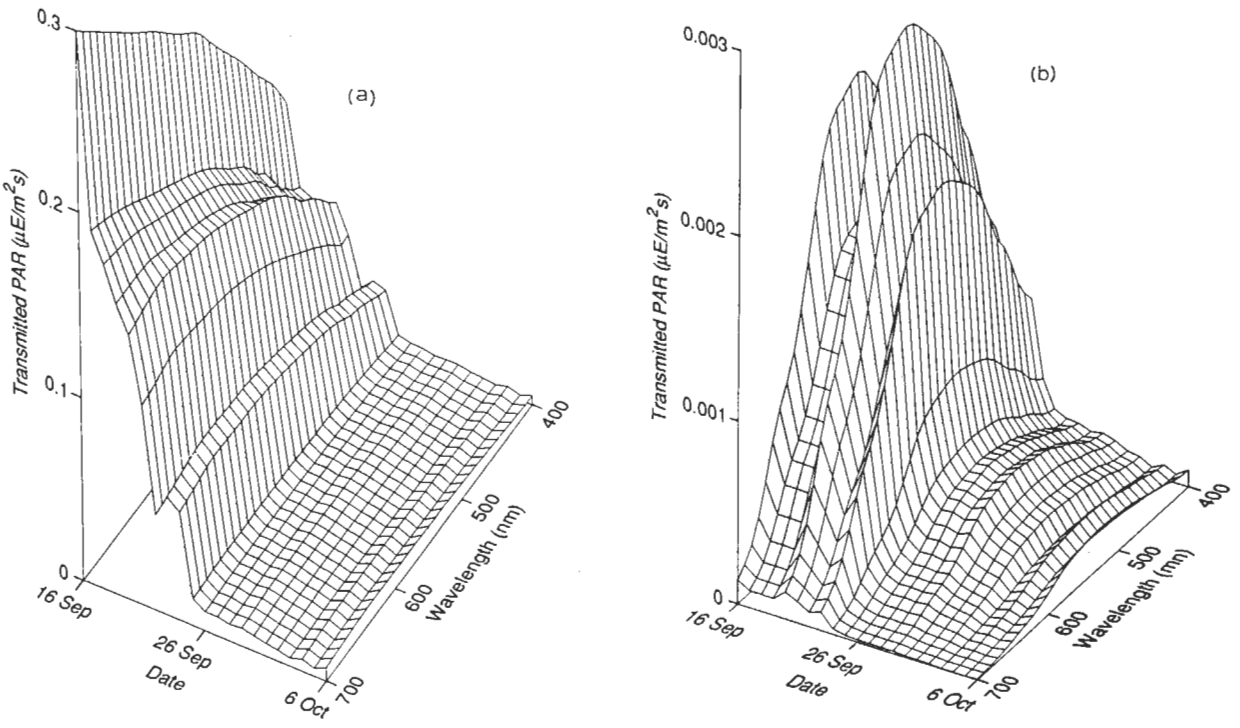

Fig. 7. Calculated estimates of spectral transmitted PAR (400–700 nm) from 16 September to 6 October for (a) young ice, and (b) multi-year ice. Note that the vertical scale for the young ice in Fig. 6a is two orders of magnitude larger than the vertical scale for the multiyear ice in Fig. 6b.

by a gradual downward trend due to the decline in incident irradiance. During this period daily values of total PAR (Table 2) declined from 70 to 3 $\mu E/m^2s$ under the young ice and from 0.6 to 0.05 $\mu E/m^2s$ under the multi-year ice. Investigations of photosynthetic activity in Antarctic sea ice have found optimal light levels for ice algae of 2–10 $\mu E/m^2s$ (Soo Hoo et al., 1987) with activity occurring at light levels as low as 0.3 $\mu E/m^2s$ (Palmisano and Sullivan, 1983). Studies in the Arctic have found that critical photon fluxes are in the 5–8 $\mu E/m^2s$ range (Cota, 1985; Gosselin et al., 1985; Barlow et al., 1988). Because of this we believe that the light transmitted through young thin ice played a significant role in the observed fall bloom.

Conclusions

As the air temperature drops at the end of the summer, surface water freezes, the ice cools and brine volume decreases, all of which increases scattering and consequently increases ice albedo. Even more important is the first snow of winter which causes a sharp jump in albedo. A 0.10-m snowcover is optically thick, making it impossible to distinguish between blue ice, white ice and young ice underneath it at visible and near-infrared wavelengths. Temporal changes are most pronounced for refreezing leads, as albedos can increase from 0.1 to 0.8 over the course of a few days. Snow-free young ice can act as a "skylight", transmitting biologically significant amounts of short-wave radiation to the ocean even during fall. Preliminary BDRF results confirm the finding of Grenfell and Perovich (1984) that for rough surfaces and high detector zenith angles, albedos can provide at least a first-order estimate for the interpretation of remote sensing data.

Future work is needed examining light transmission through the ice, with particular emphasis on the link between transmitted radiation and biological activity. High-quality measurements of the

TABLE 2

Summary of input parameters and model results of light transmission calculations for young ice and multiyear ice

The four sky types are (1) clear, (2) partly cloudy, solar disk clearly visible, (3) cloudly, solar disk barely visible, (4) completely overcast, solar disk not visible; albedo, transmittance (T) and transmitted PAR (TPAR) are bulk values integrated from 400 to 1000 nm

Day	Incident (μE/m^{2}s)	Sky type	Young ice					Multi-year				
			H_s (m)	H_i (m)	Albedo	T	TPAR (μE/m^{2}s)	H_s (m)	H_i (m)	Albedo	T	TPAR (μE/m^{2}s)
16-Sep	73.1	3	0.000	0.000	0.05	0.95	69.50	0.028	1.62	0.95	0.0085	0.580
17	50.6	4	0.000	0.030	0.08	0.90	45.60	0.028	1.62	0.95	0.0085	0.400
18	50.6	4	0.000	0.060	0.11	0.86	43.30	0.028	1.62	0.95	0.0085	0.400
19	50.6	4	0.000	0.100	0.14	0.80	40.50	0.028	1.62	0.95	0.0085	0.400
20	85.6	1	0.005	0.130	0.48	0.47	40.00	0.028	1.62	0.95	0.0085	0.680
21	66.7	2	0.005	0.150	0.49	0.46	30.40	0.028	1.62	0.95	0.0084	0.520
22	46.7	2	0.010	0.156	0.64	0.32	14.90	0.028	16.2	0.95	0.0083	0.360
23	59.9	1	0.010	0.163	0.64	0.32	19.00	0.028	1.62	0.95	0.0084	0.470
24	55.7	1	0.010	0.170	0.64	0.32	17.50	0.055	1.62	0.97	0.0039	0.200
25	32.1	1	0.030	0.171	0.82	0.14	4.55	0.055	1.62	0.97	0.0039	0.120
26	31.1	2	0.040	0.184	0.85	0.11	3.35	0.063	1.62	0.97	0.0032	0.092
27	31.7	3	0.040	0.191	0.85	0.11	3.38	0.063	1.62	0.97	0.0032	0.095
28	27.8	4	0.040	0.198	0.85	0.11	2.95	0.061	1.62	0.97	0.0034	0.086
29	30.4	4	0.040	0.204	0.85	0.11	3.20	0.061	1.62	0.97	0.0034	0.094
30	27.8	1	0.040	0.210	0.86	0.11	2.92	0.069	1.62	0.97	0.0028	0.073
01-Oct	22.8	4	0.040	0.217	0.86	0.11	2.37	0.069	1.62	0.97	0.0028	0.059
02	20.2	4	0.040	0.223	0.86	0.11	2.09	0.069	1.62	0.97	0.0028	0.052
03	15.2	4	0.040	0.230	0.86	0.10	1.56	0.084	1.62	0.97	0.0021	0.029
04	23.6	1	0.040	0.236	0.86	0.10	2.41	0.084	1.62	0.97	0.0021	0.045
05	15.2	4	0.040	0.242	0.86	0.10	1.54	0.083	1.62	0.97	0.0021	0.029
06	26.7	2	0.040	0.248	0.86	0.10	2.70	0.083	1.62	0.97	0.0021	0.051

spectral irradiance and biological activity in and under the ice are of prime importance. Such measurements can then be used to develop comprehensive theoretical models relating ice structure, optical properties and biological activity.

Acknowledgements

The author wishes to thank Dr. D.A. Meese, for here assistance in the field measurements and for her biological insight, and Dr. A.J. Gow for providing Fig. 1. This work was funded by the Office of Naval Research Contract Number N0001489WM24004.

References

Barlow, R.G., Gosselin, M., Legendre, L., Therriault, J.-C., Demers, S., Mantoura, R.F.C. and Llewellyn, C.A., 1988. Photoadaptive strategies in sea ice microalgae, Mar. Ecol. Prog. Ser., 1488: 792–798.

Buckley, R.G. and Trodahl, H.J., 1987. Thermally driven changes in the optical properties of sea ice. Cold Reg. Sci. Tech., 14(2): 201–204.

Burt, W.V., 1954. Albedo over wind roughened water, J. Meteorol., 11: 283–290.

Cota, G.F., 1985. Photoadaptation of high arctic ice algae. Nature, 315: 219–222.

Dirmhirn, I. and Eaton, F.D., 1975. Some characteristics of the albedo of snow. J. Appl. Meteorol., 14: 375–379.

Dunkle, R.V. and Bevans, J.T., 1956. An approximate analysis of the solar reflectance and transmittance of a snow cover. J. Meteorol., 13: 212–216.

Gast, P.R., 1960. Solar radiation. In: C.F. Campen et al. (Editors), Handbook of Geophysics, New York, N.Y.

Gosselin, M., Legendre, L., Demers, S. and Ingram, R.G., 1985. Responses of sea ice microalgae to climatic and fortnightly tidal energy inputs, Can. J. Fish. Aquat. Sci., 42: 999–1006.

Grenfell, T.C. and Maykut, G.A., 1977. The optical properties of ice and snow in the Arctic Basin. J. Glaciol., 18: 445–463.

Grenfell, T.C. and Perovich, D.K., 1981. Radiation absorption coefficients of polycrystalline ice from 400–1000 nm. J. Geophys. Res., 88: 7447–7450.

Grenfell, T.C. and Perovich, D.K., 1984. Spectral albedos of sea ice and incident solar irradiance in the Southern Beaufort Sea. J. Geophys. Res., 89: 3573–3580.

Iqbal, M., 1983. An Introduction to Solar Radiation. Academic Press, New York, N.Y., 390 pp.

Kuhn, M., 1985. Bidirectional reflectance of polar and alpine snow surfaces. Ann. Glaciol., 6: 164–167.

Lackman, G.M., Guest, P.S., Davidson, K.L., Lind, R.J. and Gonzalez, J., 1989. CEAREX/Polarbjoern Meteorology Atlas, 545 pp., Monterey.

Maykut, G.A. and Perovich, D.K., 1987. The role of shortwave radiation in the summer decay of a sea ice cover. J. Geophys. Res., 91: 7032–7044.

Maykut, G.A. and Untersteiner, N., 1971. Some results from a time dependent, thermodynamic model of sea ice. J. Geophys. Res., 76: 1550–1575.

Palmisano, A.C. and Sullivan, C.W., 1983. Sea ice microbial communities (SIMCOS). I. Distribution, abundance, and primary production of ice microalgae in McMurdo Sound in 1980. Polar Biol., 2: 171–177.

Perovich, D.K., 1989. A two-stream multi-layer, spectral radiative transfer model for sea ice. CRREL Rep. 89-15, 17 pp.

Perovich, D.K. and Grenfell, T.C., 1981. Laboratory studies of the optical properties of young sea ice. J. Glaciol., 27: 331–346.

Smith, R.C. and Baker, K.S., 1981. Absorption coefficients of the clearest natural waters. Appl. Opt., 20: 177–184.

Schlosser, E., 1988. Optical studies of Antarctic sea ice. Cold Reg. Sci. Technol., 15(3): 289–293.

Soo Hoo, T.B., Palmisano, A.C., Kottmeier, S.T., Lizotte, M.P., Soo Hoo, S.L. and Sullivan, C.L., 1987. Spectral light absorption and quantum yield of photosynthesis in sea ice microalgae and a bloom of Phaeocystis Pouchettii for McMurdo Sound, Antartcia. Mar. Ecol., 33: 175–189.

Steffen, K., 1987. Bidirectional reflectance of snow at 500–600 nm. Large Scale Effects of Seasonal Snow Cover. IAHS 166: 415–425.

Taylor, V.R. and Stowe, L.L., 1984. Reflectance characteristics of uniforma earth and cloud surfaces derived from NIMBUS-7 ERB. J. Geophys. Res., 89: 4987–4996.

Tucker, W.B., III, Gow, A.J. and Weeks, W.F., 1987. Physical properties of summer sea ice in the Fram Strait. J. Geophys. Res., 92: 6787–6803.

Warren, S.G., 1982. Optical properties of snow. Rev. Geophys. Space Phys., 20: 67–89.

Weller, G., 1972. Radiation flux investigation. AIDJEX Bull., 4: 28–30.